

To be submitted to the *Astrophysical Journal*  
Draft of May 28, 2005

## Resolving the Effects of Rotation in Altair with Long-Baseline Interferometry

D. M. Peterson<sup>1</sup>, C. A. Hummel<sup>2,4</sup>, T. A. Pauls<sup>3</sup>, J. T. Armstrong<sup>3</sup>, J. A. Benson<sup>5</sup>, C. G. Gilbreath<sup>3</sup>, R. B. Hindsley<sup>3</sup>, D. J. Hutter<sup>5</sup>, K. J. Johnston<sup>4</sup>, & D. Mozurkewich<sup>6</sup>

### ABSTRACT

We report successful fitting of a Roche model, with a surface temperature gradient following the von Zeipel (1924) gravity-darkening law, to observations of Altair made with the Navy Prototype Optical Interferometer (NPOI). We confirm the claim (Ohishi, Nordgren, & Hutter 2004) that Altair displays an asymmetric intensity distribution due to rotation, the first such detection in an isolated star. Instrumental effects due to the high visible flux of this first magnitude star appear to be the limiting factor in the accuracy of this fit, which nevertheless indicates that Altair is rotating at  $0.90 \pm 0.02$  of its breakup (angular) velocity. We confirm the apparent oblateness found by the PTI interferometer (van Belle, et al. 2001) and show that the true oblateness is significantly larger owing to an inclination of the rotational axis to the line-of-sight of  $\sim 64^\circ$ . Of particular interest, we conclude that instead of being substantially evolved as indicated by its classification, A7 VI-V, Altair is only barely off the ZAMS and represents a good example of the difficulties rotation can introduce in the interpretation of this part of the HR diagram.

*Subject headings:* Stars: rotation, Stars: individual ( $\alpha$  Aql), Techniques: interferometric

---

<sup>1</sup>Department of Physics and Astronomy, Stony Brook University, Stony Brook, NY 11794-3800  
email: DPeterson@astro.sunysb.edu

<sup>2</sup>European Southern Observatory (ESO), Casilla 19001, Santiago 19, Chile  
email: CHummel@eso.org

<sup>3</sup>Naval Research Laboratory, Code 7215, 4555 Overlook Ave. SW, Washington, DC 20375  
email: pauls@nrl.navy.mil, tom.armstrong@nrl.navy.mil, hindsley@nrl.navy.mil

<sup>4</sup>U.S. Naval Observatory, 3450 Massachusetts Ave. NW, Washington, DC, 20392-5420

<sup>5</sup>U.S. Naval Observatory, Flagstaff Station, 10391 W. Naval Observatory Rd., Flagstaff, AZ 86001-8521

<sup>6</sup>Seabrook Engineering, 9310 Dubarry Rd., Seabrook, MD 20706

## 1. Introduction

Altair (variously  $\alpha$  Aql, 53 Aql, HR 7557, HD 187642, of spectral type A7V or A7VI-V) is one of the brightest stars in the Northern sky, sharing membership in the “Summer Triangle” with two other notable A stars. Unlike Vega and Deneb, Altair shows a rather diffuse spectrum which was early recognized to be due to a large projected rotational velocity variously estimated at  $242 \text{ km s}^{-1}$  (Uesugi & Fukuda 1982),  $217 \text{ km s}^{-1}$  (Royer et al. 2002), and  $200 \text{ km s}^{-1}$  (Abt & Morrel 1995). These estimates of its projected velocity, a lower limit for the true rotational velocity, are already a significant fraction of the breakup velocity, estimated near  $400 \text{ km s}^{-1}$ .

Altair has become a significant object in understanding the atmospheres of main sequence stars at masses near but above that of the Sun. Specifically, Altair and  $\alpha$  Cep are the two hottest stars showing Ly $\alpha$  and C II emission, taken as indicators of a chromosphere (Simon, Landsman, & Gilliland 1994; Walter, Matthews, & Linsky 1995). The absence of these indicators at earlier spectral types is taken to mean that significant convection disappears at this point on the upper main sequence. We note that  $\alpha$  Cep also has a high projected rotation velocity with estimates of  $246 \text{ km s}^{-1}$  (Uesugi & Fukuda 1982),  $196 \text{ km s}^{-1}$  (Royer et al. 2002), and  $180 \text{ km s}^{-1}$  (Abt & Morrel 1995) listed.

Altair’s known high rotation rate has promoted attempts to measure the geometrical effects of rotation over the years, starting with the Intensity Interferometer (Hanbury Brown, Davis, & Allen 1974). However, it was not until the near-IR observations with the Palomar Testbed Interferometer (PTI; Colavita et al. 1999) by van Belle, et al. (2001) that a significant flattening was detected. Comparison to classical (von Zeipel 1924) Roche models showed the flattening was completely consistent with the observed projected rotation.

Although this agreement between theory and observation is nothing short of epochal, it is incomplete. Oblateness, interpreted through Roche theory, displays the same degeneracy between equatorial velocity and tilt (inclination) as the apparent rotation velocity: one determines the quantity  $v_{eq} \sin i$  well, but not the two separately. Nor can one determine the sense of rotation, pro- or retrograde. Besides providing a test of the flattening predicted by theory, oblateness measurements do yield the position angle (PA) of the angular momentum vector, the projection of that vector on the plane of the sky.

In addition to flattening, von Zeipel (1924) predicted that for moderate rotation stellar disks would display variable surface temperatures, hotter on the rotational axes and cooler at the equator. Specifically, if one defines a local effective gravity accounting for centrifugal acceleration, then the local effective temperature is related to the effective gravity as  $T_{eff}^4 \propto g_{eff}$  which is referred to as “gravity darkening”. With sufficient rotation and at intermediate

inclinations, gravity darkening predicts that stellar disks will display asymmetric intensity distributions.

As we describe below, this prediction is of great interest in the field of optical interferometry. Asymmetric intensity distributions produce significant imaginary components in the visibilities, usually represented as a non-trivial “phase angle”. Recently developed techniques for recovering a closely related quantity, “closure phase” (Baldwin et al. 1996; Benson et al. 1997), are now being applied to the first round of stellar objects, (e.g., Wittkowski et al. 2001).

Among the first objects observed by the Naval Prototype Optical Interferometer (NPOI; Armstrong et al. 1998) in this mode was Altair. Although originally proposed as a follow-up on the oblateness observations, the object was scheduled for observation after the 3-way beam combiner was implemented, allowing measurement of closure phase around one complete triangle. Examination of the phase data immediately revealed the intermediate phase angles, unambiguously signaling the presence of an asymmetric intensity profile (Ohishi et al. 2003).

Using a model consisting of a limb-darkened disk and a bright spot, Ohishi, Nordgren, & Hutter (2004) demonstrated both the previously discovered oblateness and the necessity of including asymmetries in the intensity distribution. They argued that the probable interpretation was that of rotational flattening and gravity darkening.

In the meantime we have become aware of some limitations in those data due to inadequate corrections for “deadtimes” in the avalanche photodiode detectors (APDs) which affect the interpretation of this data set. We therefore reconsider that data set here using a subset that is relatively immune to the detector problems, a full implementation of von Zeipel’s theory (von Zeipel 1924) for the model fitting and redoing the reductions in a way that dramatically reduces noise in the bluest channels. We find that a Roche model rotating at 90% (angular velocity) of breakup and inclined  $\sim 64^\circ$  from pole-on fits the observations with high fidelity.

We show that the parameter that sets the overall temperatures scaling for the model, the effective temperature at the poles,  $T_p$ , is close to 8700 K for this model, and the polar surface gravity is correspondingly fairly high. This suggests that Altair is less evolved than one might naively expect from its spectral type and luminosity classifications.

In this model the equator is 1850 K cooler than the pole. Given that the model includes both polar brightening and a long equatorial swath of low intensity, this is a complex intensity distribution, and the agreement with the observations is a strong endorsement for the simple von Zeipel (1924) theory.

Below, we describe the new reductions, give a brief review of Roche theory and then present the fits. We note that the existence of large amounts of surface at near solar temperatures suggests that the role of Altair (and perhaps  $\alpha$  Cep?) in defining the high temperature end of convection on the main sequence may need to be reconsidered. We also note the recent announcement that Altair is a low amplitude ( $\delta$  Sct) pulsating star (Buzasi et al. 2005) which may give hope that asteroseismology will be able to put useful limits on any gradient of the angular velocity in the outer envelope.

## 2. Observations

Altair was observed on four nights, 25–27 May and 1 June of 2001, with the NPOI. These are the same observations used by Ohishi et al. (2003) and Ohishi, Nordgren, & Hutter (2004). We refer the reader to those papers for a journal of observations and a description of the observing details, but we briefly reprise them here. We have focused here on the data set obtained May 25, 2001. This is by far the largest set of data, while the other data do not increase the range of hour angles observed in the first night.

The observations used the Astrometric West (AW), Astrometric East (AE), and West 7 (W7) stations, forming a triangle of interferometric baselines with lengths of 37.5 m (AW–AE), 29.5 m (W7–AW), and 64.4 m (AE–W7). The backend combined these three input beams to produced three output beams, with one baseline on each. The output beams were dispersed into 32 spectral channels covering  $\lambda\lambda 443 - 852$  nm, although the bluest four channels ( $\lambda\lambda 443 - 460$  nm) of the W7–AW output were not functioning.

The Altair observations were interleaved with observations of a visibility calibrator,  $\zeta$  Aql (A0V), about  $12^\circ$  away on the sky. We estimated its uniform-disk angular diameter  $\theta_{\text{UD}}$  in two ways. The more straightforward was to use the color–magnitude–diameter calibration of Mozurkewich et al. (1991) based on observations with the Mark III interferometer. From the  $(R - I)$  index and  $V$  magnitude (0.00 and 2.99, respectively; Johnson et al. 1966), we estimate a uniform-disk diameter  $\theta_{\text{UD}}$  of 0.83 mas at  $\lambda 800$  nm.

The second method was to use a similar color–magnitude–diameter relation based on  $(V - K)$  and  $V$  (Mozurkewich et al. 2003), also derived from Mark III data, that produces the limb-darkened diameter  $\theta_{\text{LD}}$  and then to multiply by the ratio  $\theta_{\text{UD}}/\theta_{\text{LD}}$  calculated from the expected limb darkening for a star of the same type as  $\zeta$  Aql. The  $(V - K)$  color (0.07; Johnson et al. 1966) and  $V$  magnitude result in  $\theta_{\text{LD}} = 0.90$  mas. We integrated the monochromatic limb-darkening coefficients from Van Hamme (1993) for a star with  $T_{\text{eff}} = 9500$  K and  $\log g = 4.1$  over the same 800 nm band of the Mark III used by Mozurkewich et al. (2003). The resulting integrated limb-darkening coefficient  $u$  is 0.28, which in turn results in  $\theta_{\text{UD}} = 0.87$  mas. We therefore adopted  $\theta_{\text{UD}} = 0.85 \pm 0.02$  mas as the estimated diameter of  $\zeta$  Aql. The uncertainty of the visibility amplitudes due to the uncertainty in the calibrator diameter is negligible on the two shorter baselines, but ranges from 1% to 3% on the 64 m baseline. Simulations of the effects of rotation in  $\zeta$  Aql over possible inclinations indicated that its closure phase can rise in the blue but will never reach  $2^\circ$  and can be of either sign depending on position angle. In particular phase errors from this source are always small compared to the observational errors, channel by channel, and have been ignored.

### 3. Data reduction

#### 3.1. Incoherent integration

The NPOI observes interference fringes by modulating the optical path on the delay line for each array element, using a triangle-wave pattern at a frequency of 500 Hz. The resulting modulation of the intensity is detected in 8 bins evenly spaced over one fringe in each channel by Avalanche Photo Diodes (APD). The phase of the intensity modulation changes on time scales of milliseconds since the fringe tracker employed by NPOI tracks the envelope of the (bandwidth limited) fringe packet rather than the fringe phase.

The data in the delay bins were processed to produce five data products at each wavelength: the complex visibility and squared visibility modulus  $V^2$  for each baseline, and the triple product  $|V_1||V_2||V_3| \exp(i\phi_{cl})$ , where  $|V_i|$  is the amplitude of the complex visibility on baseline  $i$ . The closure phase  $\phi_{cl} = \phi_1 + \phi_2 + \phi_3$ , where  $\phi_i$  is the phase of the complex visibility on baseline  $i$ . Although the baseline phases themselves are affected by atmospheric turbulence, those effects cancel in the sum of three phases around a closed triangle, so the closure phase preserves information about the source structure. These data products are produced for each 2 ms cycle of delay modulation. In the standard incoherent integration as described by Hummel et al. (1998), the squared visibilities and complex triple products are summed to provide average values in one second intervals.

#### 3.2. Coherent integration

We employed a new algorithm for the coherent integration of the complex visibilities of the NPOI first presented by Hummel et al. (2003). Compared to the incoherent integration of the squared visibilities, coherent integration achieves a higher SNR of the averages due to the larger number of photons detected in a coherent sample of the fringe. We have exploited this fact to recover meaningful results from all NPOI spectrometer channels, while the channels on the blue side of about 560 nm had been usually discarded in incoherent reductions due to the insufficient number of photons detected during the instrumental coherent integration time of 2 ms. For the coherent integration time we selected 200 ms, and the resulting complex visibilities were both combined to form complex triple products and transformed individually into squared amplitudes of the modulus. Every ten samples of these quantities were then averaged (averaging real and imaginary part of the complex triple products separately) for a total integration time per data point of 2 s.

The alignment of the raw visibility phasors necessary before integration in order to

avoid detrimental coherence losses was performed as follows. Two steps are necessary to rotate the phasors onto a common fringe in order to enable a phase tracking algorithm.

First, average power spectra of the channeled visibility as a function of delay were computed for 10 ms intervals. Their maxima, corresponding to the group delays of the fringe packets, are not zero but have a typical RMS on the order of one micron as the NPOI group delay fringe tracker tries to center the fringe, but does not lock onto its phase.

Second, from the deviation in position of the fringe from the estimated geometrical value, which is non-zero and has a typical RMS on the order of  $10\ \mu\text{m}$  due to atmospheric refractive index fluctuations, we estimated the differential amount of air and thus the phase shift between the peak of the envelope of the fringe packet and the nearest fringe peak. In other words, this phase is the phase of the complex Fourier transform of the visibility as a function of wavenumber. The modulus of this transform peaks at the value of the group delay. The phase of the transform at this delay is called the group delay phase.

We converted the group delay phase to a delay using the mean wavelength of the white-light fringe, and added it to the group delay. Rotation of the visibility phasors of different channels by an angle corresponding to the ratio of this delay value and the wavelength of the spectrometer channel will align them on the same fringe. At this point, the algorithm implements a photon-noise limited off-line fringe phase tracker enabling the use of much longer coherent integration times.

### 3.3. Phase bootstrapping

We used an important modification of the above procedure by applying the phase bootstrapping method, a design feature of the NPOI interferometer (Armstrong et al. 1998). It exploits the fact that the sum of the fringe delays along a closed loop of baselines is zero (if the same fringe is identified on each baseline). Therefore, if a long baseline in a multi-telescope array sees a low contrast fringe due to, e.g., object extension, and this baseline involves two telescopes which are at the same time involved with other telescopes of the array on much shorter baselines seeing much higher fringe contrast, the fringe delay of the long baseline can be computed from the fringe delays on the shorter baselines which are "bootstrapping" the long one. In the simple case of the observations described on Altair, the fringe delay on the long 64 m W7–AE baseline is just the difference between the fringe delays on the shorter AE–AW and W7–AW baselines.

### 3.4. Averaging and editing

The 2 s data points are edited for outliers as described by Hummel et al. (1998). The final averaging is done over the full length of a pointing (called a scan at NPOI) which lasts typically 90 s. The computation of the formal errors also follows Hummel et al. (1998), except that we have implemented a different approach for the complex triple products based on a suggestion by D. Buscher (priv. comm.). Under simple assumptions the error of a complex triple product is described by an error ellipse which has one axis aligned with the triple product phasor. Assuming this we compute the error of the triple product as the error of the imaginary and real parts of the mean after applying a rotation of all phasors by the mean triple product phasor. The errors of amplitude and phase of the triple product are then equal to the error of the real part and the error of the imaginary part divided by the respective amplitudes.

### 3.5. Detector Non-linearity

A source of systematic error comes from deadtime in the pulse counting electronics controlling the Avalanche Photodiode (APD) detectors. These systems saturate at about 1 MHz and display significant non-linearity in the apparent count rates as they near this limit. The nominal design of the detector systems included a  $\tau = 200$  ns deadtime, but we have subsequently found that not only do those time constants vary significantly, channel to channel, but also that in a given channel they depend on the mean signal level because of the effects of heating. We believe that it will be possible to model and remove these effects, but some effort is involved, which we will report on in the future. Unfortunately, these problems were not recognized at the time the Altair observations were made.

However, we believe that through a rather unique set of circumstances the phase and some of the amplitude measurements acquired during the 2001 observations are to first order free of the effects of these non-linearities. One reason was that during these observations only three stations were in use and the three spectrographs recorded single baseline data.

The other reason was that the amplitude and phase measurements from each channel were accomplished with a simple Discrete Fourier Transform. By dithering the optical delay at a frequency of  $\omega$  the signal was modulated according to

$$I(t) = I_0 [1 + V \cos(\omega t + \phi)] \tag{1}$$

where  $V$  is the (instrumental) amplitude of the visibility and  $\phi$  the instantaneous phase. The



detector system responded to the modulated signal according to

$$N(t) = \frac{QI(t)}{1 + \tau QI(t)} \sim N_0(t) - \tau N_0^2(t) + \dots \quad (2)$$

Where  $Q$  is the quantum efficiency,  $N(t)$  is the apparent pulse rate and  $N_0(t) = QI(t)$  is the true photon detection rate. In the linearized form we assumed  $\tau N_0 \ll 1$  which for a 300 kHz count rate, typical of the wider red channels on the higher visibility baselines, is adequate to 1% or better. Substituting equation 1 into 2, clearing the quadratic cosine using the half angle formula and collecting terms, this becomes

$$N(t) \sim \bar{N}_0 [1 - \tau \bar{N}_0 (1 + V^2/2)] + \bar{N}_0 V (1 - 2\tau \bar{N}_0) \cos(\omega t + \phi) - \frac{\tau \bar{N}_0^2 V^2}{2} \cos(2\omega t + 2\phi) \quad (3)$$

where  $\bar{N}_0 = QI_0$ . A DFT at the dither frequency now extracts an amplitude different than the nominal  $\bar{N}_0 V$  (and after division by the nominal mean signal produces an estimate that can differ significantly from the true visibility amplitude). However, the phase comes through the process unaffected, as do the frequencies of the minima in the visibility amplitudes. By floating the overall amplitudes in the data reduction (see below) we retain the important spatial scale information contained in the minima. But the most important conclusion is that the phases may be assumed to be essentially free of detector induced biases.

### 3.6. Visibility calibration

The degradation of the measured visibilities due to atmospheric and instrumental effects is measured, as with all interferometers, by observing calibrator stars with diameters as small as possible to reduce uncertainties in the visibility estimates for them. As shown by Hummel et al. (1998), the NPOI visibility amplitudes sometimes show a negative correlation with the RMS of the delay line motion which is related to the seeing. But at other times, instrumental effects which correlate with time or other systematic effects which correlate with position on the sky (e.g., hour angle) can dominate the visibility variations. Therefore, formal photon-noise based visibility errors usually require the addition (in quadrature) of a calibration error which is derived from the residual visibility variations of the calibrator after calibration. For the amplitude calibrations, we smoothed the calibrator visibilities with a 20 min Gaussian kernel in hour angle, and obtained calibration errors ranging from about 4% at the red end to 15% at the blue end of the spectrometers. For the closure phase, we used the same smoothing technique but applied to the calibrator phases as a function of time.

This standard NPOI procedure, however, did not yield satisfactory results as was recognized during the model fitting with respect to the consistency of the fits to successive scans. One can already see this from the results of Ohishi, Nordgren, & Hutter (2004) (their Fig. 6), where amplitudes can be systematically high or low with the important characteristic that the deviation is very consistently independent of wavelength. The effect is exacerbated by the fact that due to the brightness of Altair, the formal amplitude errors are quite small. The reason for the scan-to-scan variations is most likely the same as for the residual variations of the calibrator after calibration, except that there is no perfect correlation due to target and calibrator not being at the same location in the sky. (Past experience has shown that visibilities do correlate quite well if the calibrator is very near the target.) Therefore, we allowed the calibration for each scan and baseline to float by applying “achromatic” calibration factors to improve the fit between data and model. We will discuss the implications for the model fitting in Section 4. Finally we note that an error in the calibrator star diameter produces chromatic errors across the NPOI spectrometer as do uncompensated deadtime corrections, neither of which can be removed by the calibration factors.

## 4. Modeling

### 4.1. Roche Spheroids

The theory for the equilibrium shapes and surface properties of rotating stars was first presented 80 years ago (von Zeipel 1924) assuming solid body rotation and a point source gravitational potential. This model has proved quite successful in describing the figures of stars in close binary systems, where tidal effects to first order produce the same distortions as rotation (Collins 1989).

We use that model here, but note its limitations. First, there is no *a priori* reason that stars should rotate as solid bodies, and the surface layers of the Sun have long been known to rotate differentially. However, among the early results of helioseismology was the discovery that the transition from the outer convection zone to the inner radiative layers coincided with an abrupt transition to solid body rotation (Spiegel & Zahn 1992). Since early-type stars have radiative envelopes and relatively small (in radius) convective cores, one might expect solid body rotation to be a good approximation for the external layers of early type stars.

There has been some observational support for this expectation. Reiners & Royer (2004b) have analyzed the rotational profiles of a large number of A stars looking for evidence of differential rotation following a solar-type latitudinal dependence. In the 78 stars for which the determination could be made, they found 4 objects where peculiarities were seen which might be from differential rotation (or other causes). However, 95% of the line shapes were fully consistent with solid body rotation.

In addition there is the long known consistency between the largest rotational velocities measured in the early-type stars and the predicted maximum rotation velocities associated with “equatorial breakup” (Frémat 2005). In recent decades (e.g., Tassoul 1978) it has been demonstrated that rotation laws other than rigid rotation do not generally impose maximum rotation velocities.

The second limitation, one which we will spend some time on, involves the exponent in the  $T_{eff} - g_{eff}$  relation ( $g_{eff}$ , the effective gravity, includes centrifugal terms). In the original work von Zeipel (1924) considered the case of a fully radiative envelope, deriving the well known “gravity darkening” relation  $T_{eff} \propto g_{eff}^{0.25}$ . Lucy (1967) reconsidered the problem in fully convective stars, deriving a much reduced gravity dependence,  $T_{eff} \propto g_{eff}^{0.08}$ . Other approximations lead to other exponents (see Reiners 2003, for references). In our nominal calculations we adopt the original von Zeipel (1924) prescription. As we shall show, the Altair observations bear significantly on this issue.

Even in the limit of rigid rotation, the von Zeipel (1924) theory is only first order in rotation rate. Distortions of the interior figure, allowing some gravitational quadrupole contribution can be expected as rotation rates approach breakup. That is even more likely if there are significant deviations from solid body rotation, even if confined to the inner convective regions.

Probably even more relevant are the effects of radiation pressure, which is treated simplistically in the theory, and stellar winds. Significant envelope extension due to radiation can be expected in the low effective surface gravity regions of rapidly rotating stars. And we would certainly expect a dramatic increase in mass loss at the equator, both due to enhanced convection as gas temperatures decrease into the solar and sub-solar regime. We ignore all these effects here, except to acknowledge the limitations inherent in this theory.

## 4.2. Roche Models

We have constructed a suite of programs to evaluate the run of specific intensity across the surface of a Roche spheroid. The definitions of the various angles are from Collins (1963). Otherwise, we follow the prescription for the surface figure and the notation given by Hardorp & Strittmatter (1968) with one exception: following the discussion by Hardorp & Scholz (1971) we take the polar radius,  $R_p$ , as a fixed parameter. Specifically we do not allow it to be a function of the fractional rotation.

The modeling requires that we specify six quantities: the ratio of the angular rotation to that of breakup,  $\omega = \Omega/\Omega_b$ , the inclination (or tilt) of the rotational axis,  $i$ , defined such that  $i = 0$  is pole-on, the position angle,  $PA$ , of the pole on the sky (measured North through East), the angular diameter of the polar axis,  $\theta_p$ , the effective temperature at the pole,  $T_p$  and the surface gravity, or more commonly the logarithm of the surface gravity (cgs), at the pole,  $\log g_p$ . From the relations in the cited references it is then possible to calculate the (dimensionless) radius,  $R$ , of the star for a given stellar latitude,  $\theta$ , and hence the surface gravity  $g_{eff}$  and effective temperature ( $T^4(\theta) = T_p^4(g_{eff}/g_p)$ ) at that latitude (see Hardorp & Strittmatter 1968, for the definition of  $g_{eff}$ ).

In practice we need to solve the inverse problem: given a point on the sky,  $(\alpha, \delta)$ , determine whether the point is on the stellar disk and if so what the corresponding latitude and radius are. We have solved this problem explicitly using simple iteration, and first and second order versions of Newton-Raphson iteration. The routines (written in the “C” language) are quite flexible, reasonably fast and freely available (from the first author).

The properties of Roche models for isolated rotating early-type stars have recently been

reviewed by Domiciano de Souza et al. (2002), who use a slightly different but completely equivalent parameterization. Those authors summarize some of the results from their models for massive stars, which have provided a useful check on our own routines.

Note that for stars with good parallaxes like Altair, specifying the polar surface gravity and angular diameter is equivalent to specifying the mass and linear (polar) radius. These in turn fix the breakup angular velocity,  $\Omega_b^2 = (8/27)GM/R_p^3$ , along with the equatorial and projected velocities (when the inclination is specified). Finally, it is useful to recall the relation between the polar radius and equatorial radius at breakup angular velocity:  $R_{e,b} = 3/2R_p$ . According to this first order theory the maximum rotational flattening is 2/3.

### 4.3. Model Atmospheres

The model definition is completed by specifying the specific intensity at each point on the surface at each look angle and wavelength. As noted by the early authors, plane-parallel model atmospheres are entirely adequate in the context of Roche models for stars on and near the main sequence. The only exception is that these models develop a cusp at the equator at critical rotation velocity. However, the cusp does not appear until fractional rotation velocities of  $\omega = 0.99$  or larger and, as we have indicated, the breakdown of the plane-parallel approximation is only one of several problems with the model in this limit.

### 4.4. Implementation of Roche code

The Roche code consists of a library of functions written in C, with a main function enabling its use as standalone software and a wrapper enabling it to be called from within the NPOI standard data reduction software OYSTER. The Roche spheroid parameters are part of the standard hierarchical model format of OYSTER and are passed to the Roche code along with pointers to the extensive tables of linear, logarithmic, and square-root law monochromatic limb darkening coefficients for a grid of Kurucz model atmospheres as published by Van Hamme (1993). The Roche code, with the additional input of the  $(u, v)$  coordinates, computes the visibilities for a grid of wavelengths supplied by OYSTER, which are subsequently integrated over the NPOI bandpasses.

The fitting of the model parameters (except for the gravities) utilizes the Marquardt-Levenberg algorithm (Press et al. 1992) implemented in OYSTER, with the derivatives computed numerically. In addition to the visibility and phase measurements the reductions were also constrained to reproduce the observed V magnitude. This provided particularly

strong constraints on the polar effective temperature.

## 5. Discussion

### 5.1. Model Fitting

The analysis proceeded with few complications. In particular, a close examination of the  $\chi^2$  surface indicated no unusual morphology, and indeed the iterations converged to the same final solution independent of our starting guess, whether from larger or smaller values of the parameters. Our final solution, given in column 2 of Table 1, is based on the triple phases and triple amplitudes only, the latter with an overall floating multiplier for each scan as described above. The reduced  $\chi^2$  for this solution is still a bit large, which we attribute to some residual non-grey problems of unknown origin in the amplitudes, as shown in Figure 1. The fit to the closure phases, Figure 2, on the other hand is remarkable, showing no trends with wavelength or hour angle.

Because of the residuals in the triple amplitudes we have decided to take a conservative stance with regard to our error estimates. We have run a separate reduction using the squared visibilities for the individual baselines in place of the triple amplitudes. This solution, which has a substantially larger reduced  $\chi^2$ , reflecting the larger residuals in the amplitudes of the individual baselines, is summarized in column 4 of Table 1. Our adopted errors, shown in column 3, are the difference between these two solutions.

The fairly large  $\chi^2$  for our best model requires comment. As we have indicated, the problem is that the formal errors on the data, particularly the amplitudes, are very small due to the very high signal levels. From the variation of the calibrators we know the unmodelled errors in the amplitudes are larger than this. A rough estimate of those errors, which were not included in the solution, suggests the underlying  $\chi^2$  is closer to 1.5, although the floating amplitude multipliers make an exact estimate difficult. This is still higher than desirable, but we feel the error estimates we provide adequately characterize the quality of the fit.

Figure 3 shows how Altair appears projected on the sky. The intensity distribution at 500 nm, as would be seen for example by an interferometer, is color encoded: blue for high intensity, red for low intensity. Except for limb-darkening, this is also a temperature encoding. The range in intensities, a factor of 18, is about a factor of 2.5 more than would be expected for a non-rotating star of this spectral type.

Included in Table 1 is the integrated color as calculated by the models. Although we force all models to reproduce the observed V magnitudes, as described above, this constraint does not automatically mean the colors will be reproduced. The fact that the colors do agree with the measurements is a significant consistency check on the models, particularly given that the range of temperatures across the surface could produce a wide range of colors

25–May–01 Triple Amplitudes

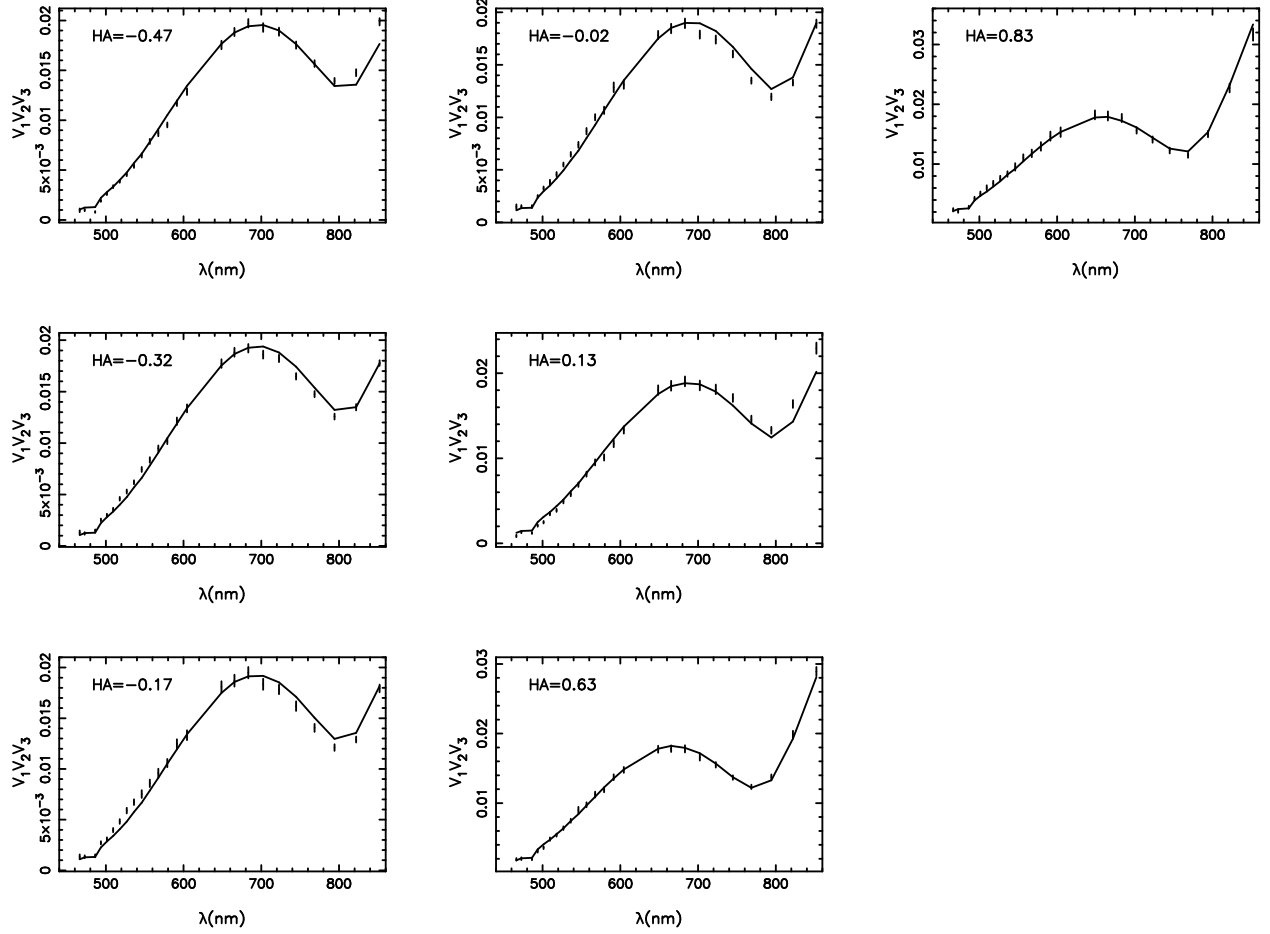


Fig. 1.— Triple amplitudes as fit by best Roche model. Error bars of  $\pm\sigma$  are shown. The analytic fits (solid line) include a constant multiplicative renormalization.



25-May-01 Triple Phases

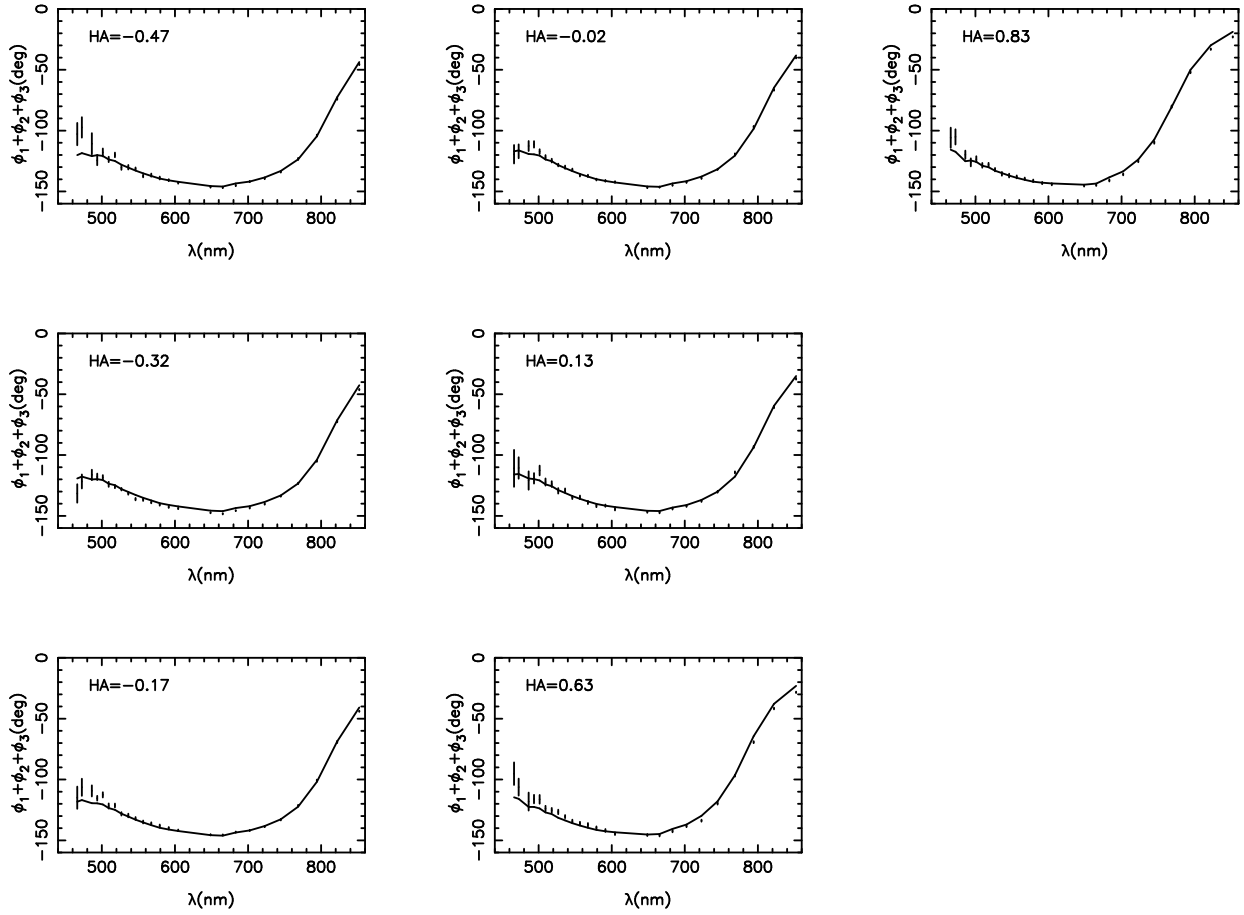


Fig. 2.— Triple phases as fit by the best Roche model. No renormalization has been applied.

# Altair $i=63.9$

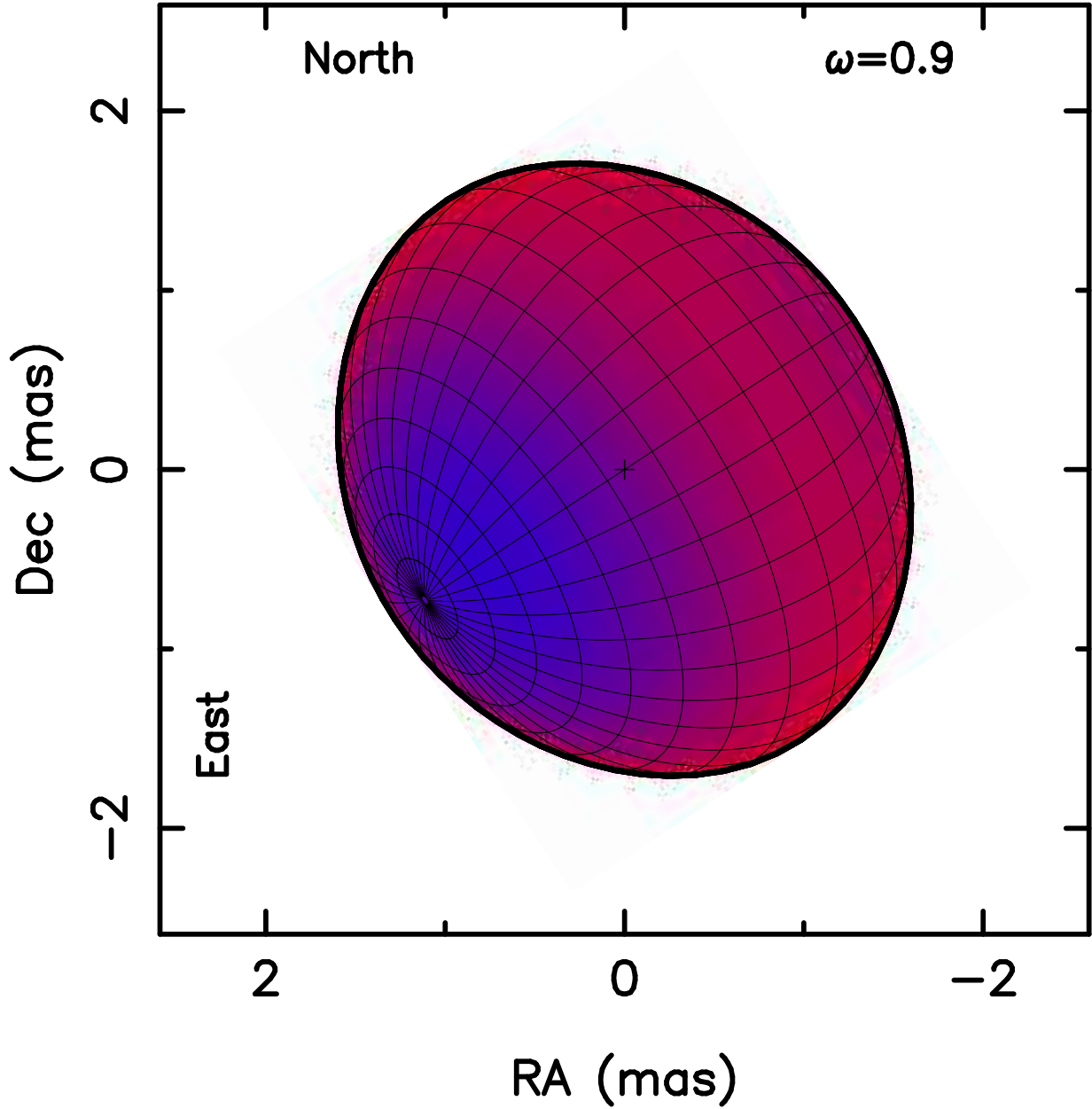


Fig. 3.— A false-color rendering of Altair's visible surface. Intensity at 500 nm increases from red to blue. Except for the effects of limb-darkening, this is also a map of temperature.

depending on the weighting. A number of ancillary parameters derived from the adopted fit are given in Table 2 and are discussed further in the §6.

## 5.2. Comparison with previous results

As noted, Altair has been the subject of a number of interferometric measurements over the years, most notably by the PTI array (van Belle, et al. 2001). The diameter determinations are not simply comparable, even if we consider only the projected major and minor axes of our model, since the PTI observations were fit to the physical dimensions of a Roche model, which included limb-darkening but not gravity darkening. Still, our determination of an equatorial radius of  $1.97 R_{\odot}$  seems in reasonable accord with their quoted  $1.88 R_{\odot}$ .

More problematic are the reported position angles of the rotational pole. First, we note that in a preliminary report of this work (Peterson, Hummel, Pauls, et al. 2004) the pole is off by  $180^{\circ}$  due to a sign error. More complicated is the disagreement between the position angle from the PTI measurements,  $-25^{\circ} \pm 9$  and our  $123.2^{\circ} \pm 2.8$ . Examination of the measurements tabulated in that paper (van Belle, et al. 2001) suggests that the identification of the baselines with the data have been reversed: the measured visibilities for the NW baseline have been incorrectly identified as from the NS baseline and vice-versa. If so the correct position angle would be obtained by reflecting the PTI result through the bisector of the two baselines. Doing this predicts a position angle of  $115.9^{\circ}$ , in complete agreement with our result.

Recently Reiners & Royer (2004b) have reported the determination of Altair’s equatorial rotational velocity,  $v_{eq} \leq 245 \text{ km s}^{-1}$ . They analyzed the star’s rotational broadening profile to determine the first two zeros of its Fourier transform, the ratio of which has been shown by Reiners (2003) to depend on the equatorial velocity rather than the usual  $v \sin i$ . This is a new approach to measuring total velocities in stars, and it is difficult to know how much weight it should be given. One notable aspect of that analysis was the adoption of an exponent for the gravity darkening law ( $\beta \sim 0.09$ ) that was about  $\frac{1}{3}$  that of the von Zeipel (1924) value. We discuss this aspect of calculating rotationally distorted stars next.

## 5.3. Gravity Darkening

While we have several lines of reasoning, described above, that lead us to believe that solid body rotation is valid for these models, the situation is not so clear with regard to the

exponent on the gravity darkening law,  $T_{eff} \propto g_{eff}^\beta$ . The classical work of von Zeipel (1924) would seem to apply to an A star, even one somewhat evolved, yielding  $\beta = .25$ . However, convection does occur in late A stars and particularly in the photosphere where it competes with radiation in carrying the flux. It is then important to note that Lucy (1967) has shown that for small distortions the appropriate coefficient in fully convective envelopes is closer to  $\beta \simeq 0.08$ .

This leaves matters in a somewhat uncertain state. On the one hand, there are stars in the transition region between having fully convective and fully radiative envelopes, Altair arguably one of them, and there is no obvious guidance in choosing an appropriate value for this parameter. On the other hand, even where the envelopes are unambiguously in either one of those states or the other, the classical results apply under rather different circumstances which we next discuss.

Both the von Zeipel (1924) and Lucy (1967) results treat rotation as a perturbation. However, in the radiative case where uniform rotation is adequate (and issues like mass loss, etc can be ignored), the quantity treated as a perturbation is the size of the quadrupole moment of the gravitational field. Since stars are centrally condensed, even for velocities approaching critical the distortions in the core are modest and one can expect that the analysis given by von Zeipel (1924) will be reasonably accurate. This has been found to be true in practice (Sackmann 1970).

For the convective case the gravity darkening exponent is found by analyzing the adiabats found in the envelopes of representative stars. Lucy (1967) quite explicitly points out that the derivation is valid only for small changes in the effective gravity. Of course, the effective gravity changes by orders of magnitude as rotation approaches critical, and it is not clear whether the exponent derived by Lucy can be used to describe gravity darkening for anything but the most modest rotation. Again, this is in contrast to the modest contribution of an induced gravitational quadrupole, even for stars rotating at breakup.

Even so, in a recent series of papers Claret (2003, and references therein) has attempted to at least deal with the issue of a smooth interpolation between these two extreme cases. He has noted that as stars evolve off the main sequence and toward the red giant branch their interior structures trace out approximately straight line loci in a  $(\log T_{eff}, \log g)$  diagram. For massive (mostly radiative) stars the slope of this line is about 0.25, and for intermediate mass stars ( $\sim 1 M_\odot$ , mostly convective) the slope is about 0.06, the two values being remarkably close to what is expected. Working with the interiors codes, Claret (2003) is able to evaluate the value of this exponent at each point in the evolutionary paths of models covering  $40 \geq M_\odot \geq 0.08$ , offering the results as appropriate exponents to use in rotating stars and stars in close binary systems.

This is a constructive suggestion for the thorny problem of choosing an appropriate gravity darkening law. However, we are not fully convinced of the leap of going from deriving a quantity based on evolutionary changes to using it to describe the effects of rotational distortion. One might make the case for small amounts of rotation or if it could be shown that rotational distortions and evolutionary effects were close to being homologous transformations from one to the other. But rotational distortions are nothing like homologous to evolutionary changes and it is not at all clear how well these ,scale=.75 “interpolations” work.

The observations reported here bear on this problem. We have tried converging our Roche models using the value  $\beta = 0.09$  adopted by Reiners & Royer (2004b). The results are shown in column 5 of Table 1. To achieve the degree of asymmetry found in the triple phase data with this low exponent value, the rotation parameter is forced to near critical rotation,  $\omega \sim 0.978$ . In turn the predicted projected rotational velocity,  $v \sin i \sim 295$  is in serious conflict with the observed value and the predicted color significantly redder than observed. Further, the reduced  $\chi^2$  is significantly worse for this fit.

We feel it is premature to use these observations to derive a “best” value of the gravity darkening parameter until the remaining amplitude residuals are better understood. However, since it is the phase measurements which are sensitive to asymmetries in brightness across the disk that are being challenged here, it does appear that the von Zeipel (1924) value for that parameter is superior to the value obtained from the Claret (2003) tables for Altair.

#### 5.4. $H_\beta$

In Figure 4 we show the blue squared visibilities of the AE-AW baseline for the 0<sup>W</sup>83 observation. The notable feature at 486nm is  $H_\beta$ , the agreement with the calculations shown in this scan, and the others not shown, is striking. This feature is nearly centered in the 486.3nm channel. In contrast  $H_\alpha$ , which has a smaller equivalent width and is split between channels at  $\lambda 665.4$  and  $\lambda 648.7$ , is much less noticable. This close agreement is a nice confirmation of the details of the model fits.

### 25-May-01 AE-AW Baseline

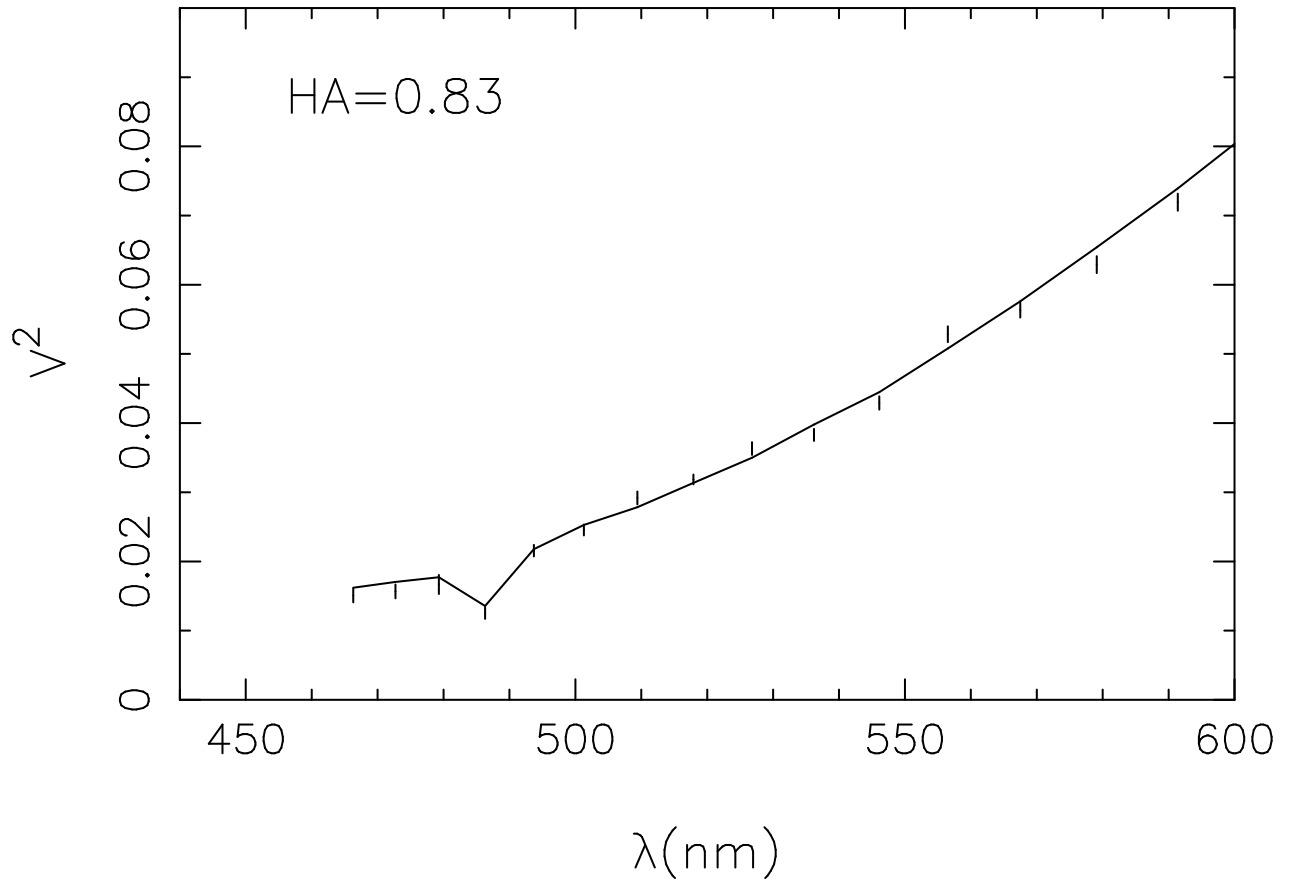


Fig. 4.— One of the observed  $V^2$ 's for the AE-AW baseline. The effect of the strong  $H_\beta$  feature in the  $\lambda 468.3$  channel is clearly evident and well matched by the model.

## 6. Conclusions

### 6.1. Imaging Altair

The primary result of these observations is, we believe, the first detection of asymmetric surface intensities on the surface of a star induced by rotation. Although we have imposed a model on the data and fit the model parameters, the simple conclusion, first reported by Ohishi, Nordgren, & Hutter (2004), is that the surface of Altair displays an extremely asymmetric intensity distribution and that the asymmetry is consistent with that expected from the known high rotation and with the previously reported oblateness (van Belle, et al. 2001). We have imaged the surface of an A star.

In Table 2 we summarize various physical parameters for the adopted model - column 4 of Table 1. Most quantities should be self-explanatory. Subscript “B” refers to the model if it were rotating at breakup. The angular diameter  $\theta_m$  is for the projected minor axis while  $\theta_M$  is for the projected major axis, i.e., the angular diameter of the equator.

### 6.2. The status of Altair

Knowing now the rotational state of Altair, we can now better answer fundamental questions such as its evolutionary status. Over the years Altair has been classified A7IV-V (e.g., Johnson & Morgan 1953), the luminosity class usually indicating an object slightly past the end of its main sequence evolution while the spectral type is that of a star having an effective temperature in the vicinity of 7800K (e.g., Erspamer & North 2003; van Belle, et al. 2001). In the context of analyzing Altair’s pulsations, it is important to know in detail its evolutionary state, mainly the extent of its core.

Fortunately, in the context of rigid rotation, this is not so difficult. Early results (e.g., Sackmann 1970) showed that two quantities were relatively insensitive to the effects of rotation: polar radius and total luminosity. The Roche model fits give polar radius directly while it is a straightforward matter to calculate the total luminosity, given a model fit.

These two quantities are not perfectly conserved. In the range of interest,  $3 M_\odot \geq M \geq 1.4 M_\odot$ , both quantities decrease with increasing rotation, approximately in proportion to  $\omega^2$ , reaching a maximum of about 6% in luminosity and 1.5% in radius (Sackmann 1970). For stars in the neighborhood of  $1.8 M_\odot$ , rotating with  $\omega^2 \sim 0.8$  we find from the Sackmann (1970) calculations that the non-rotating star would be 4% more luminous and 1% larger than our deduced polar radius.

To estimate the parameters of the appropriate non-rotating star we have used the evolutionary tables by the Geneva group (Schaller, Schaerer, Meynet & Maeder 1992). These models were calculated with modest convective overshoot ( $0.2H_p$ ). We have used the grid for a composition of  $X = 0.68$ ,  $Y = 0.30$ ,  $Z = 0.02$ .

The quantities given in Table 2 as “Non-rotating” are those estimated from the Schaller, Schaerer, Meynet & Maeder (1992) models and are quite striking. The last entry in Table 2 is the mass fraction of hydrogen remaining in the core. This is to be compared to a starting value of  $X_c = 0.68$ . Altair is almost on the ZAMS.

### 6.3. Chromospheric indicators

As mentioned in the §1, Altair, along with  $\alpha$  Cep, is one of two A7 objects in which certain ultraviolet emission lines, taken as indicators of chromospheric temperature inversions, are seen. No objects of earlier spectral type show these features and it is usually argued that these therefore represent the hottest photospheres where convection is still capable of creating such temperature profiles. The model for Altair adopted here calls that conclusion into question. As shown in Table 2 Altair has a broad swath of 6900 K gas at its equator, which is the likely source of the strong convection. We also note the recent announcement (van Belle 2005) that substantial oblateness and gravity darkening have been found in  $\alpha$  Cep, suggesting significant amounts of cool, convective gas in that object as well.

### 6.4. A $\delta$ Scuti star

As we indicated in the §1, rather than just being another rotating A star, Altair may prove a very valuable laboratory for examining the internal rotation state of a star with a predominantly radiative envelope. Buzasi et al. (2005) have announced the discovery of  $\delta$  Scuti pulsations in Altair and have identified several of the periods. This was immediately recognized as providing a potential probe of the interior structure and particularly the rotation law and an attempt has been made to identify and model the modes (Suárez, Bruntt, & Buzasi 2005). Unfortunately, not knowing the rotational state of the star and making the assumption that equator-on was the most likely orientation, Suárez, Bruntt, & Buzasi (2005) adopted a total rotation significantly lower than now seems likely. Other effects of this choice included identifying the evolutionary state as being substantially more advanced than we believe is the case. As is clear from their results, velocities above the 180–240 km s<sup>-1</sup> range they investigated lead to rapid changes in the oscillation modes.



It will not be an easy task to tap the information being provided by Altair.

The work done with the NPOI interferometer was performed through a collaboration between the Naval Research Lab and the US Naval Observatory in association with Lowell Observatory, and was funded by the Office of Naval Research and the Oceanographer of the Navy. This research has made use of the SIMBAD literature database, operated at CDS, Strasbourg, France.

Facilities: NPOI.

## REFERENCES

- Abt, H. A., & Morrell, N. I. 1995, *ApJS*, 99, 135
- Armstrong, J. T., et al. 1998, *ApJ*, 496, 550
- Baldwin, J. E., et al. 1996, *A&A*, 306, L13
- Benson, J. A., et al. 1997, *AJ*, 114, 1221
- Buzasi, D. L., Bruntt, H., Bedding, T.R., et al. 2005, *ApJ*, 619, 1072
- Claret, A. 2003, *A&A*, 406, 623
- Collins, G. W., II 1963, *ApJ*, 183, 1134, erratum, 1964, *ApJ*, 139, 1401
- Collins, G. W., II 1989, *The Fundamentals of Stellar Astrophysics* (W.H. Freeman & Co., New York), also “<http://astrwww.cwru.edu/personal/collins/astrobook/>”
- Colavita, M. M., et al. 1999, *ApJ*, 510, 505
- Domiciano de Souza, A., Vakili, F., Jankov, S., Janot-Pacheco, E., & Abe, L. 2002, *A&A*, 393, 345
- Erspamer, C. & North, P. 2003 *A&A*, 398, 1121
- Frémat, Y., Zorec, J., Hubert, A.-M., Floquet, M. 2005, *A&A*, submitted, (astro-ph/0503381).
- Hanbury Brown, R., Davis, J., & Allen, L. R. 1974, *MNRAS*, 167, 121
- Hardorp, J., & Scholz, M. 1971, *A&A*, 13, 353
- Hardorp, J., & Strittmatter, P. A. 1968, *ApJ*, 151, 1057
- Hummel, C. A., Mozurkewich, D., Armstrong, J.T., Hajian, A.R., Elias II, N.M., & Hutter, D.J. 1998, *AJ*, 116, 2536
- Hummel, C. A., Mozurkewich, D., Benson, J. A., & Wittkowski, M. 2003, in *Interferometry for Optical Astronomy II*, edited by W. A. Traub (*Proc. SPIE*, 4838), 1107
- Johnson, H. L., Iriarte, B., Mitchell, R. I., & Wisniewski, W.Z. 1966, *Comm. Lunar Plan. Lab.*, 4, 99
- Johnson H.L. & Morgan W.W. 1953, *ApJ*, 117, 313

- Lucy, L.B. 1967 ZAp, 65, 89
- Mozurkewich, D., et al. 1991, AJ, 101, 2207
- Mozurkewich, D., et al. 2003, AJ, 126, 2502
- Ohishi, N., Nordgren, T. E., Hummel, C. A., & Hutter, D. J. 2003, Astronomical Society of Japan, September Meeting, N33b
- Ohishi, N., Nordgren, T. E., & Hutter, D. J. 2004, ApJ, 612, 463
- Peterson, D.M., Hummel, C.A., Pauls, T.A., et al.. 2004, Proc. SPIE, 5941, 65
- Press, W. H., Flannery, B. P., Teukolsky, S. A., and Vetterling, W. T. 1986, Numerical Recipes in C, 2nd ed. (Cambridge Univ. Press, Cambridge)
- Reiners, A. 2003, A&A, 408, 707
- Reiners, A., & Royer, F. 2004a, A&A, 415, 325
- Reiners, A., & Royer, F. 2004b, A&A, 428, 199
- Royer, F., Grenier, S., Baylac, M.-O., Gómez, A.E., & Zorec, J. 2002, A&A, 393, 897
- Sackmann, I.-J. 1970, A&A, 8, 76
- Schaller, G., Schaerer, G., Meynet, G. & Maeder, A. 1992, A&AS, 96, 269
- Simon, T., Landsman, W. B., & Billiland, R. L. 1994, ApJ, 428, 319
- Spiegel, E. A., & Zahn, J. P. 1992, A&A, 265, 106
- Suárez, J.C., Bruntt, H., & Buzasi, D. 2005, preprint, astro-ph/0503355
- Tassoul, J.-L. 1978, Theory of Rotating Stars, (Princeton Univ. Press, Princeton NJ)
- Uesugi, A. & Fukuda, I. 1982, Revised Catalogue of Stellar Radial Velocities, Department of Astronomy, Kyoto Univ., <http://cdsweb.u-strasbg.fr/cgi-bin/Cat?III/63B>
- van Belle, G. T., Ciardi, D. R., Thompson, R. R., Akeson, R. L., & Lada, E. A. 2001, ApJ, 559, 1155
- van Belle, G. T., Ciardi, D. R., ten Brummelaar, T., et al. 2005, preprint
- Van Hamme, W. 1993, AJ, 106, 2096

von Zeipel, H. 1924, MNRAS, 84, 684

Walter, F., Matthews, L. D., & Linsky, J. L. 1995, ApJ, 447, 353

Wittkowski, M., et al. 2001, A&A, 377, 981

Table 1. Roche Model Fits for Altair

Parameter	3-Amp/ $\phi$	Errors	$V^2$ & 3- $\phi$	$\beta = 0.09$
$\omega = \Omega/\Omega_c$	0.90	$\pm 0.02$	0.88	0.978
$\theta_p$ (mas)	2.96	0.04	3.00	3.04
$T_p$ (K)	8740	140	8600	7980
$i$ (deg)	63.9	1.7	62.2	65.6
$PA$ (deg)	123.2	2.8	120.4	97.4
$\chi^2/\text{DOF}$	3.8		9.5	13.4
V (obs: 0.77)	0.765		0.765	0.76
B-V (obs: 0.22)	0.215		0.22	0.26
$V_{eq} \sin i$ (km s $^{-1}$ )	245		231	295

Table 2. Altair Physical Parameters

Quantity	Unit	Value
Rotating Parameters		
$V_{eq}$	$\text{km s}^{-1}$	273
$V_{eq,B}$	$\text{km s}^{-1}$	374
$\Omega$	c/d	2.71
$\Omega_B$	c/d	3.01
$T_p$	K	8740
$T_{eq}$	K	6890
$R_p$	$R_\odot$	1.636
$R_{eq}$	$R_\odot$	1.988
$\theta_m$	mas	3.056
$\theta_M$	mas	3.598
$\log L$	$L_\odot$	1.027
$\log g_p$	cgs	4.266
$\log g_{eq}$	cgs	3.851
Non-rotating Parameters		
M	$M_\odot$	1.78
R	$R_\odot$	1.65
$\log g$	cgs	4.25
$T_{eff}$	K	8140
$X_c$	–	0.60